Reusing 60GHz Radios for Mobile Radar Imaging

Yanzi Zhu, Yibo Zhu, Ben Y. Zhao and Haitao Zheng
Department of Computer Science, UC Santa Barbara, CA 93106, USA
{yanzi, yibo, ravenben, htzheng}@cs.ucsb.edu

ABSTRACT

The future of mobile computing involves autonomous drones, robots and vehicles. To accurately sense their surroundings in a variety of scenarios, these mobile computers require a robust environmental mapping system. One attractive approach is to reuse millimeter-wave communication hardware in these devices, *e.g.* 60GHz networking chipset, and capture signals reflected by the target surface. The devices can also move while collecting reflection signals, creating a large synthetic aperture radar (SAR) for high-precision RF imaging. Our experimental measurements, however, show that this approach provides poor precision in practice, as imaging results are highly sensitive to device positioning errors that translate into phase errors. We address this challenge by proposing a new 60GHz imaging algorithm, *RSS Series Analysis*, which images an object using only RSS measurements recorded along the device's trajectory. In addition to object location, our algorithm can discover a rich set of object surface properties at high precision, including object surface orientation, curvature, boundaries, and surface material. We tested our system on a variety of common household objects (between 5cm–30cm in width). Results show that it achieves high accuracy (cm level) in a variety of dimensions, and is highly robust against noises in device position and trajectory tracking. We believe that this is the first practical mobile imaging system (re)using 60GHz networking devices, and provides a basic primitive towards the construction of detailed environmental mapping systems.

Categories and Subject Descriptors

C.2.2 [**Computer Systems Organization**]: Computer-Communications Networks

Keywords

60GHz; RF imaging; environmental mapping; mobile radar

1. INTRODUCTION

Mobile computing is evolving. For decades, mobile computing centered around the user and her movements, whether it was on foot, or on vehicles such as buses or cars. However, the next gener-ation of mobile computing and its challenges will likely be defined in the context of a variety of autonomous mobile agents, including drones, self-driving cars, or semi-autonomous robots. Today, autonomous drones are scanning large crop fields and farm live-stock, unmanned helicopters are delivering supplies to soldiers in the field, while water-proof drones patrol the underground sewer system in Barcelona [3]. In the near future, flying drones will de-liver our mail, packages and groceries, self-driving cars will drop us off at work, and first responder robots will be first on scene to rescue victims of disasters [31].

A key challenge for the widespread deployment of these au-tonomous devices is the environmental sensing system, *e.g.* a mo-bile imaging radar system that captures the position, shape and sur-face material of nearby objects. These systems must provide accu-rate and robust information about the device's surrounding at night or in dark areas (*e.g.* tunnels), while moving at moderate speeds. Highly accurate results are critical, and errors can produce dire consequences. For example, Google's self-driving cars use maps with inch-level precisions [35], while devices that assist the visu-ally impaired must have errors smaller than 10cm [9, 22]. Finally, to be placed on a variety of autonomous devices, the imaging sys-tem should be compact, lightweight and cost-effective.

None of the existing solutions meet these needs. Traditional vis-ible light imaging systems (*e.g.* cameras) perform poorly in dark or low-light conditions, and lack the precision desired by these appli-cations. Acoustic solutions have been used successfully for rang-ing over short distances [39, 49], but are easily disrupted by back-ground noise and fail over longer distances. Prior works on RF imaging use WiFi bands to track human motion and activity [7, 8, 15, 12], detect metal objects [12], and map large obstacles [36]. But they require costly specialized hardware or large antennas unsuit-able for mobile devices. A recent project reuses WiFi communi-cation devices with multiple antennas to image objects, but its pre-cision is fundamentally limited by WiFi's large wavelength [25]. Finally, while today's millimeterwave imaging systems can offer accurate object imaging [6, 10, 34, 42], they all require specialized hardware, *e.g.* large lens radars and FMCW circuits, and do not fit the size or cost constraints of commodity mobile devices.

RF Imaging via 60GHz Networking Radios. One attractive approach is RF imaging radar that reuses commodity 60GHz net-working radios to "image" the environment by capturing 60GHz transmissions reflected by nearby objects. Such a high frequency RF radar system has several key advantages over alternatives. *First*, 60GHz links are highly directional, making them relatively im-mune to interference from environmental factors such as ambient sound or wireless interference. *Second*, 60GHz beams exhibit good reflective properties, and work reliably in a wide range of lighting conditions in both indoor and outdoor locations. *Finally*, 60GHz ra-

dios are relatively inexpensive ($< \$40$ [45, 51]), and small enough to be included in today's smartphones and tablets.

The real challenge of building accurate mobile RF imaging is achieving high accuracy within a small device. A simple rule from imaging radar theory [13], defined by eq.(1), holds for antenna size (aperture) and the optimal accuracy (radar resolution):

$$Resolution = \frac{wavelength \cdot distance}{aperture}.$$ (1)

For smartphone-sized antennas, even the most high frequency radios (5-120GHz) can produce resolutions no better than 1 meter, clearly inadequate!

Our initial work in this space explored the possibility of using device mobility to emulate a *virtual antenna array* with large aperture [52]. This design uses the mobile device as a receiver, with a decoupled transmitter either embedded in the infrastructure or "deployed" on-demand by the user, (*e.g.*, mounted on a nearby drone). By taking measurements of the same reflected signal at multiple locations and applying the *Synthetic Array Radar (SAR)* algorithm [14], the system emulates the signals received by different elements of a large antenna array. Using 60GHz beams is especially advantageous here. Since 60GHz has a carrier wavelength of 5mm (12x shorter than WiFi/cellular), a user using 60GHz links can obtain fine-grain resolution with just small movements in the measurement area [52].

Practical Limitations of SAR. The goal of our work is to design, build, and deploy an accurate mobile imaging system for practical applications. Through experiments on an experimental testbed, we quickly identified *two* fundamental limitations with the SAR approach to imaging radar in real-world mobile settings. *First*, SAR is highly sensitive to receiver trajectory tracking noise. Any deviation from the path produces significant error in the predicted points on the reflection surface. This impact becomes particularly notable when the deviation is greater than λ, the RF wavelength. Whether the receiver is a handheld device, a robot, or a flying drone, its movement is likely to deviate from the targeted straight line trajectory, and deviations are likely much greater than λ for 60GHz links, which is 5mm. *Second*, high resolution imaging via SAR requires knowledge of the beam's phase information (ϕ). But any mm-level error in the receiver's position or trajectory introduces large errors in computing ϕ, and thus using phase information actually adds large errors into the SAR imaging result.

Ensuring accurate positioning and movement tracking to the level of millimeters is difficult using commodity hardware. Thus, accurate mobile 60GHz imaging requires a new imaging approach robust to device positioning and trajectory errors.

60GHz Imaging via RSS Series Analysis. Our observation is that the SAR algorithm is sensitive to positioning errors because each error propagates when computing positions on each object's surface. As a more robust alternative, we propose an approach that identifies the location, overall shape, size and material of the target object, by comparing the measured distribution of 60GHz received signal strength (RSS) values against RSS value distributions predicted from our general surface-reflection model. Since key surface properties (*e.g.* width and curvature) are strongly correlated with reflected RSS distributions, we can accurately determine the overall surface shape of the target object. We call this approach *RSS Series Analysis*, or RSA for short. Finally, our work leverages a unique advantage of 60GHz radios – as the receiver moves and (re)aligns its beam, it reports the (strongest) receive beam direction and the corresponding RSS value [2]. Such directional RSS measurements carry ample information of the reflection surface to enable high precision imaging.

RSA is robust against small device positioning and tracking errors because unlike SAR, it does not image an object by locating the individual points on the reflected surface. Instead, RSA focuses on how the collection of these points creates a distribution of RSS values at different observation locations. Such a distribution not only captures the overall shape of the target object, but also tolerates local deviations and errors in device positioning and tracking. Using testbed experiments, we find that an RSA-based 60GHz system can achieve accurate imaging results in the presence of positioning errors as large as 10cm.

In the remainder of this paper, we present our 60GHz-based mobile imaging system. We describe techniques for automatically estimating object location, orientation, surface curvature, surface boundaries, and even the surface material of nearby objects. We also present a detailed workflow of a practical implementation of our 60GHz imaging, including techniques for detecting the presence of objects and planning the receiver movement. Finally, we use detailed experimental measurements on a local 60GHz wireless testbed to validate the utility and accuracy of our techniques. Our testbed results on 12 common household objects (of 5cm-30cm in width) show that our proposed imaging system can image these objects at a high precision (*e.g.* $\sim$5cm in object location and surface boundaries) with just small movement ($\sim$1m) by the receiver.

Limitations. Our work provides a first step in the development of high precision RF imaging (re)using 60GHz networking chipsets. Our current design has several limitations; some fundamental to the choice of 60GHz radios, while others can potentially be reduced via a better design.

First, to stay robust against device positioning/tracking errors, our RSA imaging does not use any phase information from the radio[1]. As a result, we are unable to recognize fine-grained details on an object, *e.g.* the individual keys on a computer keyboard. Instead we can identify the overall rectangular shape of the keyboard. Similarly we were unable to identify very small objects like keyrings. Improving imaging precision in the presence of device positioning errors is an area of open research. *Second*, the working range of our imaging system is determined by the underlying 60GHz radios and the object surface material[2]. While our solution does not need actual high speed transmissions, accurate RSS measurements require signals to be sufficiently stable. Using an off-the-shelf, low-cost mobile 60GHz chipset (from Wilocity), we found that the imaging range[3] is at least 10m for metal objects, and 5m for cardboard boxes (like those found in Amazon packaging). *Finally*, because 60GHz signals cannot penetrate walls or most objects, our imaging system works when both transmitter and receiver have line-of-sight to the target object. Thus to perform effective imaging, especially in 3D, mobile devices must have a way to intelligently navigate across complex spaces. This is another active research problem.

2. MOBILE 60GHZ RADAR

In this section, we set the context for mobile imaging using 60GHz transmissions. First, we begin by identifying key challenges facing mobile imaging systems, and explain why 60GHz radios provide an attractive solution. We then describe initial designs on 60GHz

---

[1] In some cases, not requiring phase can be an advantage of our system, since most COTS radios do not report phase but only RSS.
[2] Objects of different materials introduce different degree of signal loss. Metal objects in general introduce no loss while wood objects introduce 12dB loss in signal strength.
[3] Here the imaging range defines the distance between the object and the receiver, assuming the transmitter and receiver are of equal distance to the object.

imaging radar using synthetic array radar (SAR) algorithms, and the limitations they face in real deployment settings.

2.1 Mobile Imaging Radar and 60GHz

Mobile imaging radar systems face additional technical challenges compared to their traditional counterparts. Traditional imaging radars detect the position and shape of an object by emitting RF signals and analyzing the reflected signal [7, 8, 15, 12, 36, 6, 10, 34, 42]. They typically make use of specialized hardware such as FM circuits and highly directional, large dish antennas, and thus are not suitable for mobile devices. Instead, to be placed on a variety of autonomous devices from smartphones to drones, the imaging system should be severely constrained in size in both the processing hardware and the antenna, which severely limits the maximum imaging resolution (see Eq. 1). For smartphone-sized antennas ($2.5cm$ aperture), maximum imaging resolution for an object of $10m$ away is $1m$ using 120GHz transmissions or $24m$ at 5GHz. Furthermore, mobile radar systems target commodity devices, which rules out costly FM pulse circuits. Similarly, cost constraints prevent the use of fine accuracy positioning devices, or dispersion analysis for material detection (specialized transmitters).

Instead, mobile imaging radar can (re)use existing wireless networking chipsets on mobile devices, but leverage human or device mobility to greatly extend antenna aperture. This can provide resolution better than the limit defined by Eq. (1). Next, we describe key components of such a system.

Leveraging 60GHz Radios. Today's mobile devices are equipped with multiple wireless interfaces, *e.g.* cellular, WiFi, Bluetooth, and 60GHz radio[4]. Among them, 60GHz is ideal for mobile imaging for three reasons.

- Carrier wavelength of 60GHz is 5mm, over 12x shorter than WiFi/cellular. This translates into 12x smaller required antenna aperture than WiFi/cellular under the same imaging resolution.
- 60GHz's short wavelength leads to more predictable propagation, *i.e.* minimal multi-path effects and signal strength is strongly correlated to propagation distance. The system can easily detect the presence of objects by distinguishing between line-of-sight (LoS) and reflected signals.
- The object reflection profile is more stable at 60GHz. Since reflection loss is strongly correlated to object material [30], the radar system can determine the material type of the reflection surface using signal strength measurements.

Emulating virtual antenna arrays with mobility. A mobile device can emulate a large aperture virtual antenna array by moving and taking signal measurements at different positions along its trajectory[5]. This allows a small mobile device to produce high-resolution imaging results despite its small aperture antenna. For example, a device can take signal measurements along a 1 meter trajectory and achieve an (optimal) resolution at 60GHz of 15mm, from a distance of 3 meters away. Finally, user mobility also increases the system's ability to detect surface curvature of objects, as reflected signals at different locations help capture the curvature of each of the object's multiple faces.

Decoupling transmitter and receiver. Given the small size of mobile devices, the power of a radar system is limited. Under the limited power, decoupling the transmitter and receiver, a.k.a

---

[4]Qualcomm is producing low-cost 60GHz chipsets at or below previous prices of $37.5, with a range of $23m$ or more [45, 51]. HP recently released a laptop equipped with the Intel 60GHz chipset [1].
[5]Aperture of a virtual antenna array is equal to the distance traveled by the device.
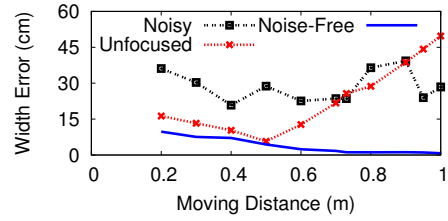

Figure 1: Experimental results demonstrate the limitations of SAR.

bistatic radar system, can significantly improve radar range over a single transceiver (monostatic) [40]. We consider a mobile radar system including the primary mobile device acting as a receiver and a decoupled transmitter. For example, a system to assist the visually impaired may include an app on the user's smartphone, and transmitters embedded in the walls or ceiling. The transmitter/receivers duties can also be split across multiple mobile devices, *e.g.* multiple drones scanning underground tunnels.

The transmitter (TX) sends 60GHz beacons that reflect off of nearby objects. Each beacon includes the angle of transmission, and if possible the transmitter's relative location to the receiver. Each RX moves and periodically scans and records signal strengths for beacons, and processes these data on the fly to identify, locate and image nearby objects.

2.2 A Synthetic Array Radar (SAR) System

Our earlier work proposed a 60GHz imaging system [52], where the receiver estimates object location and surface boundary using the Synthetic Array Radar (SAR) algorithm [14]. Applying SAR on measurements along a trajectory emulates the process where a large array focuses its narrow beam on different points of the object surface. Controlled testbed measurements achieve centimeter level accuracy in detecting object location and surface boundaries.

The SAR Algorithm. The imaging process is driven by the traditional SAR algorithm for bistatic radar [41]. TX transmits a simple sine wave, which is reflected by the object towards RX. RX measures the reflected signal at different locations as it moves. To understand SAR, consider a simple case where the object is a point. Let N represent the number of signal measurements taken by RX. The complex signal $r_i(t)$ measured at RX location i is $r_i = A_i e^{-j\phi_i}$ where A_i is the product of the transmit and receive antenna field radiation pattern and total propagation/reflection loss at i, and ϕ_i is the change in phase. Assuming signal reflection does not introduce any phase change, $\phi_i = \frac{2\pi}{\lambda}d_i$ where d_i is the total propagation distance. SAR computes the relative power $\mathcal{P}(p)$ at any point p in space using the RSS $|r_i|$ and phase shift ϕ_i at different locations: $\mathcal{P}(p) = \left|\sum_i r_i e^{j\frac{2\pi}{\lambda}\hat{d}_i}\right|$, where $\hat{d}_i$ is the distance from TX to each RX location i through the point p. If this point is a point on the object surface, *i.e.* $\hat{d}_i = d_i$, then the summation is constructive and $\mathcal{P}(p)$ is large. Otherwise because of destructive interference, the relative power becomes small. Thus SAR determines the object location and shape by searching for the strongest $\mathcal{P}(p)$ values across space.

2.3 Limitations of SAR

Existing design [52] makes two "idealistic" assumptions on device positioning: (1) TX and RX have perfect knowledge of their relative position; (2) RX moves in a perfect trajectory *e.g.* a straight line. However, in practice these two assumptions do not hold, and the imaging performance degrades significantly.
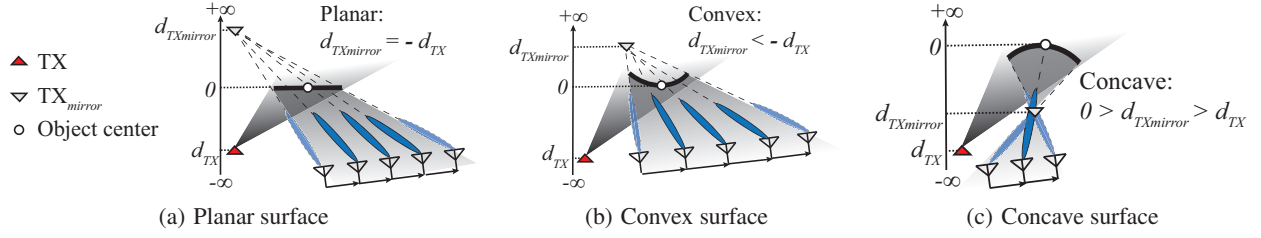
Figure 2: An abstract view of the 60GHz signal reflection and RX's signal measurements as it moves.

Limitation 1: Sensitivity to trajectory noise. It is well-known that SAR is highly sensitive to trajectory noise – when moving, RX often deviates from the targeted path, and its trajectory cannot be tracked accurately. Such noise translates into errors in computing $\hat{d}_i$ and thus affects $\mathcal{P}(p)$. The impact becomes highly visible when the error is comparable to or larger than RF wavelength λ. For 60GHz, $\lambda = 5$mm. Thus even a few millimeter deviation in trajectory can largely affect the imaging result.

We perform experiments to examine this artifact. Figure 1 plots the imaging performance in terms of the error in derived surface boundary, for different object-to-RX distances. We compare two systems: "noise-free SAR" where the RX moves in a straight line and "noisy SAR" where we introduce random deviations (up to 5mm) to the actual RX trajectory. We see that in the presence of noise, the imaging error magnifies by at least 4 folds to 40cm! We also observe that errors in TX-RX positioning have similar effect (results omitted due to space limits). SAR cannot tolerate such small errors, let alone the 10cm error typically seen from the trajectory of mobile devices like drones.

To address this problem, one may consider using motion sensors to record the trajectory precisely. But commercial sensors cannot achieve millimeter-level accuracy. For example, accelerometer reports only the acceleration of device, and the translation information can only be obtained by integrating the result twice, resulting in poor performance [38]. GPS is known to have meter-level errors. Another approach by traditional SAR is to estimate the movement noise [27]. This can be effective for aircraft radars because the movement noise comes from air turbulence and can be approximated to the level of their operating wavelength (more than 10m). But for our targeted 60GHz mobile scenarios, the movement noise is much more random and harder to predict at the millimeter level.

Limitation 2: Dependency on phase information. To achieve high resolution, SAR requires the knowledge of the phase information ϕ_i. However, since the positioning/trajectory errors will corrupt the phase transition process, using the phase information actually introduces large errors in imaging. An alternative solution is to use "unfocused" SAR which assumes $\{\phi_i\}_{i=1}^N$ are all identical, *i.e.* $\phi_i = 0$, and only uses RSS to compute $\mathcal{P}(p)$ [52]. This reduces the impact of trajectory errors, but sacrifices imaging resolution: the longer the receiver trajectory, the more the "uniform phase approximation" error amplifies and degrades imaging accuracy. Figure 1 shows that unfocused SAR performs slightly better than noisy SAR but far worse than noise-free SAR. Note that while (noise-free) SAR always benefits from longer moving distance (larger antenna aperture), unfocused SAR is highly sensitive to this parameter. After the trajectory distance exceeds some threshold, compounded error from the "uniform phase approximation" overcomes the gain of larger apertures, and imaging performance deteriorates quickly. This threshold is object dependent and hard to identify *a priori*[6],

---

[6]Our measurements show that the threshold scales linearly with the object width and RX-object distance, thus hard to identify *a priori*.

making the performance of unfocused SAR unpredictable. Similarly, existing work reported that unfocused SAR can be 10 times worse than SAR [28].

Summary. These results highlight the fact that SAR-based systems are highly sensitive to device positioning errors. Because of 60GHz's small wavelength (5mm), even small deviations in position translate into large distortions in phase transition results, and significant errors in imaging quality. Given these fundamental limitations, we must explore SAR alternatives to achieve the high accuracy demanded by next generation autonomous devices.

3. RSS SERIES ANALYSIS (RSA)

Our proposal to address these limitations is *RSS Series Analysis* (RSA), a new 60GHz imaging algorithm. Unlike SAR, RSA images an object using *only* RSS measurements recorded along the receiver's trajectory. We summarize RSA here and present the detailed algorithm in §4. RSA offers two advantages over prior work on RF imaging [25, 29, 52]:
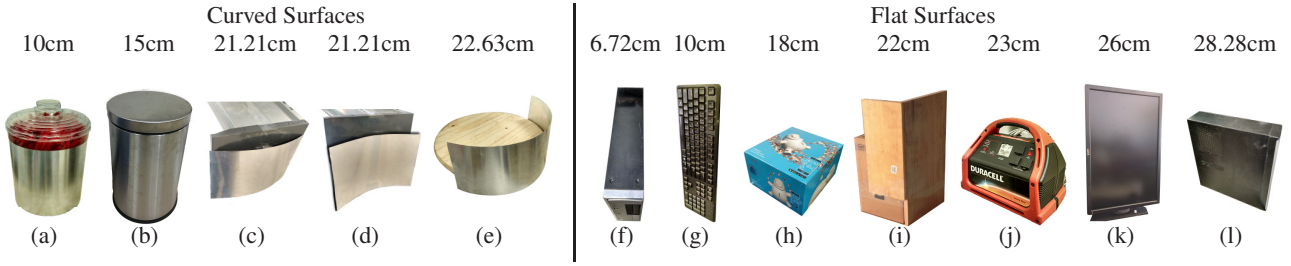
- RSA can discover a rich set of object surface properties at high resolution (cm level). These include object surface location, orientation, curvature, boundary and material.
- RSA is highly robust against device positioning and trajectory tracking noise. Testbed results show that it can tolerate deviations as large as 10cm without degrading imaging quality.

3.1 Core Concept

RSA achieves high-precision imaging by combining receiver mobility with the high directionality of 60GHz beamforming. Specifically, RSA treats each object surface as a continuous medium that reflects a directional 60GHz signal towards the directional receiver RX. As RX moves and continually (re)aligns its beam to maximize received signal strength, the measured RSS value and its receive beam direction (angle of arrival (AoA)) carry information of the object surface. By analyzing these *directional* RSS measurements across multiple RX locations, RSA recovers important properties of the object surface, including position, curvature, boundary and material. At a high level, RSA works in 3 sequential steps.

1. Surface curvature & center position. Consider a scenario in Figure 2(a) where TX points towards and reflects its beam off a flat object surface. As it moves, the directional receiver RX maximizes RSS by pointing the receive beam towards the mirror point of TX respect to the object surface, *i.e.*, TX_{mirror}. This is a hypothetical point that would have originated the signals if there was no reflection, which can be computed as the intersection of AoAs, *i.e.*, the strongest RSS direction, for different points on the RX trajectory. While in practice the AoA reported by RX might deviate slightly due to non-ideal antenna patterns, imperfect reflection and measurement artifacts, one can still locate TX_{mirror} by intersecting the series of (noisy) AoAs collected as RX moves.

Now consider the scenario where the object surface is curved, either convex (Figure 2(b)) or concave (Figure 2(c)). We can still

Curved Surfaces						Flat Surfaces					
10cm	15cm	21.21cm	21.21cm	22.63cm	6.72cm	10cm	18cm	22cm	23cm	26cm	28.28cm
(a)	(b)	(c)	(d)	(e)	(f)	(g)	(h)	(i)	(j)	(k)	(l)

Figure 3: Objects used in our experiments. The number on top of each object is the width of the object. The left five objects (a)-(e) have curved surfaces and the right seven objects (f)-(l) have flat surfaces.

locate TX$_{mirror}$ by intersecting the reported AoAs. Following the mirror and lens equation [24], a surface's curvature type is determined by its focal length f:

$$\frac{1}{f} = \frac{1}{d_{TX}} + \frac{1}{d_{TX_{mirror}}} \qquad (2)$$

where d_{TX} and $d_{TX_{mirror}}$ are defined in Figure 2. Both values are under sign convention, *i.e.*, positive if behind the object, and negative when in front of the object. The surface is convex if $f > 0$, concave if $f < 0$, plane if $f \to \infty$, and $|f|$ is half of the curvature radius. Therefore, we can identify surface curvature by computing d_{TX} and $d_{TX_{mirror}}$. This requires information of the position and surface orientation of the object center, which can be estimated by intersecting the TX center beam direction with the reported AoAs.

2. Surface boundary. Once curvature is determined, RSA detects surface boundary by exploiting the unique effect of 60GHz directionality on signal reflection. When RX is within the area of "object coverage area" (Figure 2(a)), the corresponding RSS is strong because RX can align its beam to capture the (strong) reflected signals. But when RX moves outside of this area, the quality of its beam alignment (and RSS) degrades quickly. Thus shape of observed RSS values across different RX locations is strongly correlated to the object surface boundary. Using the estimated surface curvature, center location and orientation, we can model this correlation to enable reliable detection of surface boundary.

3. Material. When a signal hits a surface, parts of it may be "absorbed," leading to a *reflection loss*. At 60GHz, this reflection loss has a strong correlation of the surface material and the incident angle [30]. In particular, the RSS of a reflected signal is the RSS of a LoS signal (of the same propagation distance) minus the reflection loss (all in dB). Once we know surface location and curvature, we can derive the reflection loss and incident angle, and thus identify the likely surface material(s).

3.2 Quantifying Correlation via Measurements

Our intuition is that RSS measurements along a trajectory are highly correlated to a number of properties of a reflection surface. We use a commodity 60GHz radio testbed (details in §6) to better understand these correlations. We experimented with twelve objects (listed in Figure 3) of different width (5cm–30cm), curvature, material (wood, metal, plastic) and surface roughness (smooth vs. rough)[7]. We varied the TX and RX locations to examine the impact of object placement.

---

[7]A surface is considered smooth if $h < \frac{\lambda}{8cos\theta}$ and rough if $h > \frac{\lambda}{8cos\theta}$ [48]. Here h is the min to max surface protuberance, $\lambda = 5mm$ and θ is the incident angle. For our objects, the plastic keyboard is "rough" and a monitor surface is "smooth."

We experimented with four movement patterns involving a 1-meter straight line trajectory in space: a drone flying[8], a user moving a mobile phone over a line, an arc, and a perfect straight line. All four trajectories use the same start and end positions, and take the same amount of time to finish. RSS measurements are taken every 1cm, leading to a total of $N = 100$ measurements per trajectory. Each experiment collects $\{RSS_i, AoA_i\}_{i=1}^{N}$, where RSS_i is the strongest RSS value as RX rotates its beam at location i and AoA_i is the corresponding receive beam direction.

Our experiments led to two key observations.

1. Strong correlation with object surface properties. Our experiments confirm a strong correlation between RSS measurements and object surface properties. We show in Figure 4 that the RSS patterns, either as RSS values or AoAs, can be used to distinguish objects of different surface curvature, surface boundary (*i.e.* width), and material. The groundtruth of focal length in Figure 4(a) is 0.6m, 0.6m, and infinity, respectively.

2. Robustness against trajectory noise. The RSS series (both RSS and AoA) are highly robust against trajectory noise. Figure 5 illustrates different views of the four trajectories, and the RSS values along the trajectories when imaging an object of 6.7cm wide. While the trajectories deviate from each other by as far as 10cm, their spatial RSS patterns align well. We experimented with other movement patterns and objects, and arrived at similar conclusions. A closer look shows that RSS values correlate most strongly with propagation distance d. But in practice, d is at least multiple meters, and trajectory errors are in centimeters. Thus trajectory errors have little impact on RSS.

While these results may not be representative, they validate our intuition that much about properties of the reflection surface can be found in RSS measurements along the movement trajectory. Next we present techniques to extract these properties from RSS data.

4. RSA IMAGING ALGORITHM

Our RSA algorithm provides highly accurate imaging results on distance, curvature, boundary, and material detection, all while tolerating positioning and trajectory errors. It takes three inputs: a sequence of RSS measurements in RSS and Angle of Arrival tuples $\{RSS_i, AoA_i\}_{i=1}^{N}$, RX's trajectory (*i.e.* RX location i) and its relative position to TX, and TX's transmit beam direction and pattern. We will discuss in §5 the procedure to obtain these inputs and the sensing process for TX to focus its beam on the object.

Imaging an object takes four processing steps on the RSS data. We estimate location and orientation of the object center, then compute surface curvature, and boundaries, and finally identify a set of potential surface materials. We first describe these key components

---

[8]Using a high-end IRIS+ drone by 3D Robotics Inc., we captured its movement trajectory when configured to fly straight.
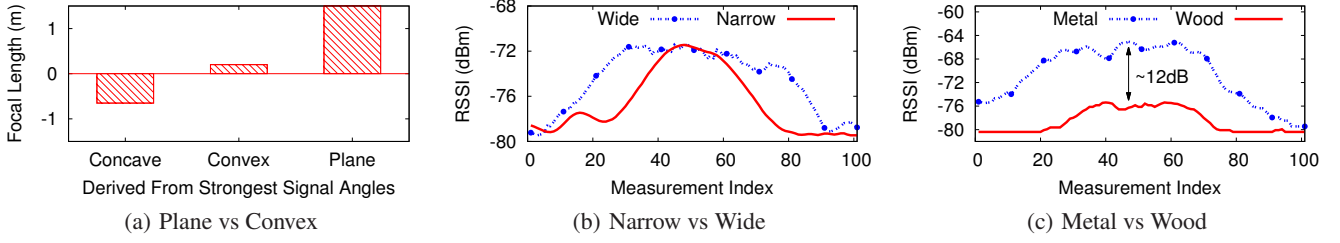
Figure 4: The observed RSS seires are strongly correlated with the object surface properties.
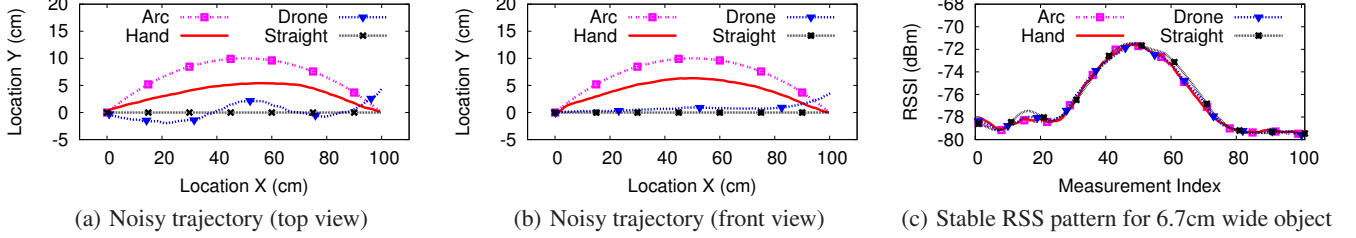

Figure 5: The measured RSS series remains stable across all four (noisy) 3D trajectories.

to image a single surface, and then the process to image multiple surfaces/objects. Finally, we describe how RSA mitigates noise from device localization, interference and RSS measurements.

4.1 Estimating Object Center & Orientation

RSA starts by computing an initial estimate of the location and surface orientation of the object center, since it is input for subsequent steps. The intuition is simple: when TX's beam covers the object evenly and TX/RX are perfectly aligned, we can locate the object surface center at the intersection of the TX beam direction and each AoA. While the TX/RX alignment is imperfect (since TX fixes its beam), the intersection with each AoA_i is still a good approximation of the reflection surface.

Like [52], RSA estimates the object center by performing a "majority vote" on the set of intersection points. Given K ($K < N$) intersection points, RX identifies a cluster of $\lfloor \frac{K}{2} \rfloor + 1$ points with the minimum mean square error (MSE) among themselves. It approximates the object center as the center of the cluster, *i.e.* the position with minimum MSE to all other points in the cluster. To generate the K intersections, RSA picks a subset of $AoAs$ from $\{AoA_i\}_i^N$ whose RSS_i is among the strongest (and above the noise level) and intersects them with the center direction of TX beam.

Since the incident and reflected angles are equal, we can compute the (candidate) direction of the object surface's principal axis with respect to each of the K AoAs. We derive the object center's orientation by computing the principal axis using majority vote over K candidates, then computing its perpendicular direction.

A key difference from [52] is that RSA iterates to improve its estimate of object center and orientation, using as input the curvature and boundary results from later steps. This helps to mitigate the impact of TX/RX positioning errors and other artifacts (§4.6).

4.2 Characterizing Surface Curvature

After object position comes surface curvature. We characterize an object's surface curvature based on the mirror and lens equation defined by eq. (2). We first compute the "TX mirror point" and then compute the focal length f from d_{TX} and $d_{TX_{mirror}}$. We compute it as the intersection of angle of arrivals for different points on the RX trajectory (Figure 2). To mitigate noise/artifacts in AoA measurements, RSA first smoothens the AoAs using a moving window,

e.g., of size 3 in our current design, then performs a majority vote on pair-wise AoA intersections to derive the mirror point.

Given the estimate of object center point and orientation, we calculate d_{TX} and $d_{TX_{mirror}}$ by projecting the TX and the TX mirror point to the principal axis (see Figure 2). If we set the object center as position 0, d_{TX} is negative and $d_{TX_{mirror}}$ is positive. RX then computes f based on eq. (2). The surface is convex if $f > 0$, and concave if $f < 0$, and $2f$ is the curvature radius. In theory, a flat/planar surface should have $f = \infty$. Yet in practical scenarios, $f > 1$ meter is sufficient to identify most objects with a flat surface.

4.3 Computing Surface Boundary

The next step is to compute the surface boundary, *i.e.*, the width of the surface if the object was projected to the plane of RX's movement trajectory. We exploit the strong correlation between the RSS sequence $\{RSS_i\}_{i=1}^N$ and the object surface, and propose a simple RSS model for surface reflection. After adding surface curvature and center location as parameters, this model generates a direct one-to-one mapping between a specific surface boundary and the sequence of RSS values captured by RX. Thus we can estimate the surface boundary by searching for a surface profile whose model-predicted RSS sequence matches those observed by RX.

A RSS model for surface reflection. We develop a new surface reflection model, which takes into account the reflection property of a "fixed-size" reflection surface. Consider the TX transmission towards the object as a collection of sharp rays, each reaching a point p on the object is reflected towards RX. Here we consider a general scattering reflection scenario where the point p uniformly scatters signals in space according to the Lambertian reflection model [26, 53]. We also consider a far-field scenario where the propagation distance is much larger than wavelength (*i.e.*, > 100 times larger). In our case, the wavelength of 60GHz is $5mm$, and the overall propagation distance in our system should be at least $0.5m$. Using the complex baseband representation under far-field approximation, the 60GHz received signal at RX location i is

$$r_i(t) = \int_{\mathbb{P}} \underbrace{\frac{\lambda \sqrt{G_p(i)} e^{-j\frac{2\pi}{\lambda} d_p(i)}}{4\pi d_p(i)}}_{\text{overall propagation}} \underbrace{\Gamma_p(i) e^{-j\phi_p(i)}}_{\text{reflection}} u(t) dp \quad (3)$$
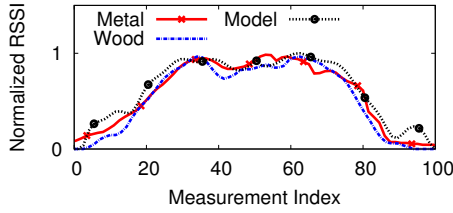
Figure 6: Comparing measured and predicted RSS patterns.

where for the pth reflected path arriving at location i, $G_p(i)$ is the product of the corresponding transmit and receive antenna field radiation pattern, $d_p(i)$ is the total propagation length, $\Gamma_p(i)$ is the amplitude reflection coefficient, $\phi_p(i)$ is the corresponding change in phase, $u(t)$ is the complex baseband transmitted signal, and $\mathbb{P}$ represents the object surface in 3D space. The key to this model is the constraint of the fixed size reflection surface, captured by the integral over $\mathbb{P}$.

Because our design targets the overall shape of the object, we simplify Eq.(3) by assuming the surface is relatively smooth, *i.e.* ignoring the fine-grained details. Therefore we consider a uniform reflection pattern: *i.e.*, $\Gamma_p(i) = \Gamma, \phi_p(i) = \phi, \forall p \in \mathbb{P}, i = 1..N$. Then we can pull out the $\Gamma_p(i)$ term, and derive RSS as:

$$RSS_i = P_t \cdot \Gamma^2 \left| \int_{\mathbb{P}} R_p(i) dp \right|^2 \quad (4)$$

where $R_p(i) = \frac{\lambda \sqrt{G_p(i)} e^{-j\frac{2\pi}{\lambda} d_p(i)}}{4\pi d_p(i)}$. Given the object curvature and center location, and locations of TX and RX(i), we can calculate $R_p(i)$. Given the object surface boundary or width, we can construct $\mathbb{P}$ and then derive RSS_i[9]. To remove the contribution of Γ which is unknown, we can normalize RSS_i across i.

We verified this model using testbed experiments on objects in Figure 3. Example results in Figure 6 show that normalization effectively separates the contribution of materials from that of the surface boundary, *i.e.* two objects of the same width but different materials have the same normalized RSS series. The measured RSS series closely matches the series predicted by our model.

Fitting Measurements to Model. We determine the surface boundary by matching the observed RSS values to a range of RSS series produced by the model. In this process, we consider a range of possible surface width values. For each candidate width w, we construct the physical surface $\mathbb{P}$, use the model to predict the (normalized) RSS series, and compare it with our (normalized) measured RSS series. To compute "similarity" between two series (or curves), we experimented with multiple metrics, including MSE, MSE of the derivatives, and MSE of the dynamic time warping algorithm [37]. Among these, MSE of the derivatives is the best:

$$\eta = 1 / \sum_{i=1}^{N} \left(\Delta_i^{model} - \Delta_i^{real} \right)^2 \quad (5)$$

where Δ_i^{real} and Δ_i^{model} are the derivatives of the normalized RSS at i using the measured values and the modeled values, respectively. This metric works well because computing surface width means detecting the two edges, which lead to fast RSS degradation at the corresponding RX locations. The RSS derivatives effectively capture such RSS variation. We leave the task of finding the optimal metric to future work.

---

[9]For efficiency, we approximate $\mathbb{P}$ as a collection of points whose interspacing $\leq$ 5mm.

Minimizing Search Space. We can significantly reduce the search space for the surface boundary size, by looking at only widths that can exist within the triangle formed by the start and end points of the RX trajectory, and the TX mirror point (see Figure 2(a)). RX can detect if the width w is large enough for the triangle to bound the reflection surface (steep dropoff in RSS before and after the surface boundaries). For very large surfaces, RX might need to extend its trajectory to detect the surface boundary. Assuming the surface is bounded by the triangle, we can estimate the maximum value of w using geometry. We then search for the true value of w starting from the max down to $1cm$ in the unit of $0.1cm$. These settings are sufficient for the target imaging precision. Going for a higher granularity adds extra computation complexity but little improvement of imaging quality. Currently our search takes less than $3s$ for all our twelve test objects using a matlab implementation on a standard MacbookPro. As future work, we can further prune the search space using sophisticated methods such as cutting planes.

Measuring Curved Surfaces. For curved surfaces, the reflected RSS series display a different pattern: a convex surface will *scatter* signals to a wider area while a concave will *gather* signals towards a smaller area (Figure 2). Thus using the above method, we will likely image a narrow, convex object as a wide object.
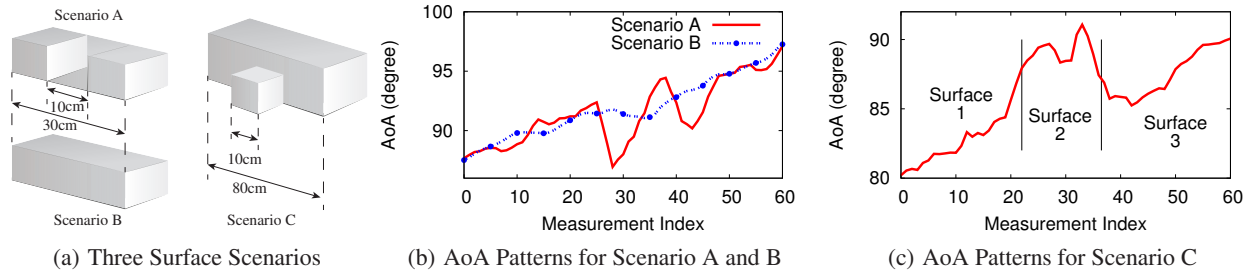
To address this, we apply a slightly different algorithm. Upon determining that the object surface is non flat, RSA computes the surface boundary using $\{R\hat{SS}(\theta)_i\}_{i=1}^N$, *i.e.* the RSS measured at a *fixed* receive beam direction θ across all positions along the RX trajectory. Here $\theta = AoA_j$, $j = \text{argmax}_{i=1..N} RSS_i$, *i.e.* the AoA of the strongest RSS across all the RX locations. Intuitively, this direction θ is parallel to the surface's principal axis, thus $R\hat{SS}(\theta)_i$ includes less contribution of surface scattering (or gathering) but more impact of surface boundary. This way, we can apply the same surface reflection model by using the curvature detection result to construct $\mathbb{P}$. In §6, we show that this method is accurate and also robust against errors in the estimated curvature radius.

4.4 Identifying Potential Surface Materials

Finally, we seek to estimate the surface material based on the reflection loss Γ^2. Existing measurement studies on 60GHz propagation and reflection have built a table of Γ^2 values as a function of the surface material and the angle of incident [30]. We can estimate the angle of incidence given the estimated surface orientation and curvature. From Eq. (4), $\Gamma^2 = RSS_i^{real} / \left(P_t \left(\frac{\lambda}{4\pi} \right)^2 \left| \int_{\mathbb{P}} R_p(i) dp \right|^2 \right)$. With Γ^2 and the angle of incidence, we can *narrow down* the material type using the reflection loss table. For example, we can distinguish metal objects (0.3dB loss) from wood (12dB loss) or plastic objects (8dB loss).

To obtain a reliable estimate of Γ^2 for flat surfaces, we select a group of the strongest RSS measurement locations, and calculate the Γ^2 as above for each location. We then compute Γ^2 as their average. This helps to mitigate noise contributed by reflection artifacts near object boundaries.

Estimating Γ^2 for curved surfaces is more challenging because as signals scatter or gather, the above calculation becomes less reliable. Our current solution is to introduce a compensation factor that approximates the impact of signal scattering or gathering. Specifically, we input the already derived object curvature and width into the RSS model, use it to generate the RSS series (ignoring Γ^2), and record the maximum RSS value, γ_{curve}. We then input the width into the RSS model but treat the surface as flat, generate the RSS series and record the max, γ_{flat}. The final reflection loss estimate is $\Gamma^2 \cdot \gamma_{flat}/\gamma_{curve}$ where $\gamma_{flat}/\gamma_{curve}$ reflects the impact of signal scattering/gathering.

(a) Three Surface Scenarios   (b) AoA Patterns for Scenario A and B   (c) AoA Patterns for Scenario C

Figure 7: Detecting and imaging multiple objects. (a) The three scenarios considered: two surfaces separated by a gap, a single continuous surface, and one small surface in front of a big one. (b) The AoA pattern changes abruptly when two surfaces are separated. (c) The AoA pattern displays three segments when a small surface is in front of a big one.

4.5 Imaging Multiple Surfaces/Objects

So far our discussion targets scenarios with a single object surface. We now discuss the feasibility of RSA for detecting and imaging multiple objects/surfaces. We consider two representative scenarios: (1) two nearby objects separated by some space; and (2) a smaller object in front of a larger one (see Figure 7(a)).

Intuitively, a key difference between single and multiple surface reflection should be the reflection angle, *i.e.*, the AoAs. Using testbed measurements, we verified that for the above two multi-surface scenarios the AoA pattern is significantly different from a single surface of the same width. For example, Figure 7(b) plots the reported AoAs as a function of the measurement location (1-60) over a 60cm RX trajectory. For an even surface of 30cm in width, the AoA pattern grows smoothly as the RX moves. But when this object is replaced by two 10cm objects separated by 10cm (same overall width), the AoA pattern changes abruptly (by $3-5°$). Similarly, Figure 7(c) plots the AoA pattern when one 10cm-wide object is placed in front of a 80cm-wide one. It is segmented into three regions, corresponding to the uncovered portions of the larger object surface on each side and the small object in the middle.

These significant changes in AoA patterns suggest that multiple objects can be detected using AoA derivatives along the trajectory. For all object scenarios we tested[10], a threshold of $3°$ can reliably detect and extract multiple objects. We can then apply the single-object based RSA to each segment to image individual surfaces of moderate sizes. The key limitation here is that our imaging system lacks the precision to image small objects and fine-grained surface details, *e.g.* individual keys on a computer keyboard. Instead, it should detect and image an Amazon package on the floor.

Above results also suggest that RSA can handle interference due to reflection from other objects. We treat the 80cm-width surface in scenario C as the background object, where our system can still identify and image the 10cm-wide object (surface 2) in the middle.

4.6 Handling Noise & Interference

We design RSA to stay robust to three types of noise or errors: *positioning error* for locating TX and RX, *trajectory noise* when RX's trajectory deviates from the ideal line, and *RSS measurement noise* caused by RF interference or background reflection.

TX/RX positioning errors. Errors in TX/RX positions can propagate to errors in locating object center point and TX mirror point. We address this by exploiting the fact that the measured RSS series is stable and strongly correlated with the object surface. After one round of imaging, RSA introduces *controlled perturba-*

tions to explore possible small shifts in center location and surface boundary values that lead to a better match between the model predicted RSS profile and measured RSS data. Specifically, it shifts the TX/RX locations by up to $10cm$ and repeats the imaging process. This iterative search stops when the similarity metric (defined by eq. (5)) exceeds some threshold, or the boundary results of two consecutive iterations differ by 1cm or less, *e.g.* convergence.

RX trajectory errors. The basic imaging algorithm assumes precise data on RX's trajectory. In practice, the movement itself is noisy – a high-end drone configured to fly a straight line can deviate by 4cm. Motion-tracking (via accelerometers or other sensors) can easily generate 10cm errors in less than a second [4, 38].

Trajectory errors can translate into errors in locating the object center and TX mirror point, and errors in RSS model. For the former, RSA denoises by applying "majority vote" across multiple RX AoA measurements (§4). For the latter, we found the impact on imaging quality to be minimal, and both RSS model and measurements are insensitive to trajectory errors $< 10cm$. In our scenarios, we configure RX to move in a line and rely on external trajectory control to keep the trajectory error less than $10cm$. In practice, any errors that do propagate will add to noise in estimates of object center and TX mirror point. These will be addressed together with any resulting noise from TX/RX positioning errors (see above).

Interference. Background reflection from other objects can be handled via the multi-surface detection and imaging process described §4.5. The bigger challenge comes from possible corruption of RSS measurement values by RF interference from other 60GHz transmissions, *e.g.*, strong signals from a LoS transmitter to RX will distort the AoA values.

If angular separation between the interfering signal and reflected TX signals is sufficiently large, RSA can eliminate interference using 60GHz directionality. As RX scans across directions, it detects and decodes signals from different sources and only uses those from TX to construct the RSS series. In rare cases where the signals are closely aligned, the interference will likely affect data transmission between TX and RX during imaging, *e.g.* high RSS but recurring packet errors. When this is detected, TX and RX can switch to another 60GHz channel or change physical location.

5. IMPLEMENTATION

We now present the detailed workflow of a practical implementation of RSA imaging. First, TX and RX determine each other's position. They scan for any objects, and once found, TX focuses its beam on the object and computes the RX movement direction and distance. RX moves, collects RSS measurements and images the object. The process does not require tight synchronization between TX and RX, only that TX signals remain consistent during imaging,

---

[10]In our scenarios, when two objects are separated, the gap ≥ 10cm. The ability to detect 10cm gaps between objects is sufficient for most mobile applications like drones.

e.g., a simple sine wave, so that RSS is stable over time. In particular, for 802.11ad [2], our sine wave based design can directly use single carrier (SC) to send consistent 0s or 1s and generate a regular sine wave, or use one of the OFDM subcarriers for imaging.

TX/RX positioning. To determine each other's location, TX and RX can exchange their locations (if known), or apply existing mobile localization/ranging techniques based on RF or acoustic signals [11, 29, 39, 49]. We can also apply 60GHz localization in addition to improve localization accuracy to centimeter-level (if TX and RX have line of sight).

60GHz localization leverages the 802.11ad bootstrapping procedure and includes two steps. First, TX (in directional mode) steers its beam in different directions and embeds its beam direction in the signal. RX (in omni-directional mode) receives signals over time and identifies the strongest signal strength r and TX beam direction α. If a LoS path exists between them, then RX can compute its distance to TX d from r (using the 60GHz Friis propagation model [19]). To detect whether LoS exists, TX compares α and r with those estimated by the external localization technique. If the discrepancy is large, especially if d is larger, the path is reflected. Otherwise, LoS exists and TX locates RX via α and d. Next, TX transmits in α direction. RX enters directional mode and scans for the strongest signal. RX can locate TX using the strongest receive direction at RX and d.

Object Sensing & RX Movement Planning. TX and RX use the above two steps of 60GHz localization to sense nearby objects and compute the appropriate RX trajectory. There are two modifications from the sequence above. In step one, instead of reporting only the strongest RSS, RX reports a list of TX beam directions where the RSS exceeds the noise level. After pruning the list by removing the LoS directions, the remaining represent reflected signals. From these directions, RX identifies a set of TX beam directions $\{\alpha^k\}_{k=1}^T$ that TX should focus on based on their beam radiation patterns and steering granularity. If an object is too wide to be covered by a single TX beam, RSA can image the object by having TX steering sequentially in multiple segments and stitching the image results, or by TX modifying its antenna radiation pattern to form a wider beam (if possible).

In the second step, TX slowly steers its beam in each of these directions while RX measures AoA for each α^k direction. Ideally, for each α^k, RX should move perpendicularly to the corresponding AoA to detect object width. Furthermore, RSA uses the intersection of α^k and AoA to approximate the object location and thus the total propagation distance d_p. The projected RX movement distance is then the width of the TX beam pattern at distance d_p, which is sufficient to discover the object surface shape. Together the recommended path and distance allow RX to create a virtual antenna array large enough to discover the object's surface while minimizing the travel distance.

Object Imaging. TX focuses its transmission on each specific direction (while embedding the beam direction in its signal). As RX moves, it collects RSS measurements using the 802.11ad *antenna alignment* procedure. Collecting the (RSS, AoA) tuple across multiple directions (§4.3 and §4.6) does not require extra measurements, and is done by modifying 802.11ad to report additional data. Since for phased array, full-scope beam steering takes less than 1ms[11], RX can perform real-time measurements as it moves, even when TX rotates its beam across multiple directions to image multiple objects. Finally, RX analyzes the data to image the object(s).

Latency. We expect the imaging delay is dominated by those of RX movement and RSA data analysis. For latter, our current implementation finishes in less than 3s and can easily be further optimized, *e.g.*, using convex optimization during iterative search (§4.6).

6. EVALUATION

We evaluate RSA in practical settings using off-the-shelf 60GHz radios. We study its utility and imaging quality in the presence of device localization and trajectory errors and background reflections. We also examine its error tolerance, and its sensitivity to different system/hardware configurations. Finally, we compare RSA with SAR and unfocused SAR, and perform a multi-object case study by emulating drones locating a target object using RSA.

6.1 Testbed and Experimental Setup

We consider two types of 60GHz beamforming radios. The first uses a pair of Dell D5000 dock (as transmitter) and 6430u laptop (as receiver), both equipped with a low-cost Wilocity 60GHz chipset designed for indoor mobile communications. The chipset uses a 2×8 rectangular antenna array, and operates under the IEEE 802.11ad standard [2]. Unfortunately, the chipset does not expose RSS values and the corresponding beam directions. Thus we use it only for understanding the range of our 60GHz imaging design when implemented on 802.11ad networking radios (§6.2).

The second and our main imaging testbed uses two HXI Gigalink 6451 60GHz radios, designed for outdoor communications. Since there are no suitable 60GHz steerable antenna arrays on the market, we emulate beam steering by setting a horn antenna (of $10°$ 3dB beamwidth) on an electronic controlled mechanical rotator. The horn antenna's main lobe pattern closely align with that of a 10×10 array with 1dBi elements and 21dBi gain, and the rotator physically adjusts the beam direction in units of $0.15°$. The HXI radios use the On-Off-Keying modulation to generate sine waves in random on-off periods and reports RSS every 50ms. We note that under the same environment, the RSS of the HXI link is actually 17dB[12] weaker than that of the Wilocity chipset. This is because our HXI radio transmits at 0dBm and the cable that connects the horn antenna to the radio introduces 23dB loss (in order to enable mechanical antenna rotation).

The results of HXI radios with horn antennas should generalize to phased arrays, because our emulation matches phased arrays in three key aspects. *First*, 60GHz signal strength is largely determined by directionality and signal patterns of the main beam lobe (the side lobe is 13.26 dB weaker), and our horn antenna's main lobe pattern closely aligns with that of a 10x10 array [51]. *Second*, because 60GHz propagation is stable over time (verified by others [23, 50] and our own measurements), at each location RX can accurately measure RSS along different directions despite its slow beam steering speed. *Third*, the fine granularity of our rotator allows us to emulate beam steering of phased arrays, *e.g.* in units of $1 - 3°$ required by the 802.11ad standard [5].

Experiment Setup. Our experiments take place in a classroom of size 8m×12m with concrete walls. We place an object in the middle of the room with LoS to both TX and RX. We move both TX and RX to study imaging range and angle. By default, TX is 2m away from the object and RX is 3.5m away. We tried other distances with little impact on results as long as the total propagation path (from TX to object and then to RX) does not exceed the radio range. By default, the testbed steers beam at a $1°$ granularity.

---

[11]Phased array beam steering delay is as low as 50ns [47]. Scanning 360° in the steps of 1° takes 18μs.

[12]The HXI radios have 0dBm transmit power, 25dBi antenna gain per radio and 23dB cable loss due to the use of rotator. To compare with, the Wilocity chipset has 10dBm transmit power and 17dBi antenna gain per radio.

We consider two types of RX movement: human waving smartphone and drone flying. The mechanical beamsteering means we cannot perform imaging in real time. Instead, we record five trajectories per type (by marking on paper) from actual movement of human users and our Iris drone, and use them to drive RSS measurements on our mechanical beamsteered radio. We align the trajectories so that the start and end points are 1 meter apart. Whether it's a user waving the device or a flying drone path, the maximum trajectory errors against a straight line are roughly $10cm$. To follow a specific moving trajectory, we mark the trajectory on the floor and pinpoint the receiver to each trajectory point using a plumb-bob.

We implemented the 60GHz localization mechanism (discussed in §5) for TX and RX. Across multiple scenarios, the measured TX/RX localization error is consistently between 2 and 6cm. We broaden our tests by adding random 2-6cm TX/RX position errors to our data analysis. In total, we have 60 noise instances per object/scenario to obtain statistically significant results.

Test Objects.   Like existing works on radar imaging [25, 36, 21, 20], we evaluate the utility and accuracy of our proposed design by imaging real objects of different size, curvature, and material. In addition to the objects listed in Figure 3 which are of 5cm-30cm in width, we also test smaller objects including a keyring and a small wrench (2.5cm in width). From these we seek to identify objects that our system can accurately image and those that it cannot.

6.2   Imaging Range & Angle

We first use the Wilocity radios to verify the working range of our 60GHz imaging system when implemented using today's 802.11ad mobile devices. For a pair of TX and RX, we block the LoS path between them, forcing the link to search and use NLoS paths, *i.e.* the reflection path. Using objects of different materials as the reflector, we measure the maximum propagation path length (TX to object to RX) such as TX can successfully transmit a 100MB file to RX. The path length is 20m for strong reflection material like metal, and 10m for weak reflection material like cardboard boxes (used for Amazon packaging). Assuming that TX and RX are of the same distance to the object, the corresponding imaging range (from object to RX) are 10m and 5m, respectively. We note that in our measurements the RSS is sufficient to support high speed communication (385Mbps) at these distances. When it comes to imaging, the RSS requirement can be much lower as long as the resulting RSS measurement is accurate. This means that the actual imaging range can be much longer.

As discussed earlier, due to extra cabling loss, our HXI link is 17dB weaker despite its stronger antenna gain. As a result, the imaging range is less than half of the Wilocity link, and we have to move the devices closer than we expect. Again this is due to artifacts of our testbed configuration.

Impact of Imaging Angle.   Like [25], we found that the imaging quality depends on the imaging angle, defined by the relative location of TX to the object and the trajectory of RX. Specifically, to identify the object, TX's beam should cover the object and the reflected signal should reach RX along its trajectory. Our system addresses this issue by performing object sensing and RX movement planning before running actual imaging (as discussed in §5). This also helps to reduce the amount of movement required to detect the overall object shape. For example, we have tested our algorithm by varying the object orientation relative to TX, *i.e.* the angle of incident, between $30°$ and $45°$, and found that it always provides an ideal RX movement trajectory, and the subsequent imaging results remain consistent across these experiments. We also found that RX's actual movement can deviate from the ideal trajectory by at least $7°$ without noticeable impact on imaging quality.
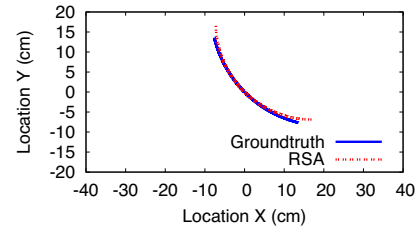

Figure 8: Result of imaging a curved surface.

6.3   Imaging Precision

Position/Curvature/Width.   Table 1 lists RSA's overall imaging results in terms of errors in object center position and orientation, detected curvature type, shape deviation[13], and errors in surface boundary (width) estimation. We list the median and max values across all experiments while varying TX/RX position errors (60 instances) and RX trajectories (10 instances, 5 user-waving, 5 drones). The results for human waving and drone flying are consistent, so we did not isolate them.

We see that in the presence of position/trajectory noises, RSA achieves centimeter-level accuracy across all the objects, flat or curved. In terms of center locations, the max error is below 4cm for metal flat surfaces, and slightly larger (6-9cm) for curved surfaces and other materials (due to weaker reflection). Note that the depth of the object can be calculated based on the estimated object center position and the location of RX, which we found has a max error of $6cm$. The orientation error is always $< 1°$. RSA detects the curvature type accurately, and characterizes the shape of the surface within $0.68cm$ deviation for flat surfaces and $< 6cm$ for curved surfaces. The maximum error in surface width estimation is bounded $4.5cm$. Figure 8 plots the imaging result of a curved surface which captures the overall curved shape while being a slightly wider than the actual object.

Material.   Using existing measurements on 60GHz reflection [18, 30], we built a reflection database of 39 materials. We added the profile of cardboxes using our own measurements. Using RSA estimated reflection loss and incident angle, we identify from the database the top three material candidates. Table 2 lists the result for four flat objects of different types (metal, plastic, wood and cardboard) and two curved objects, where RSA can successfully narrow down the material type.

Observed Limitations.   We also make the following key observations from our experiments. *First*, RSA reuses COTS 60GHz radios to image objects in the presence of device movement and tracking noises. To be robust to such noises (which existing designs like SAR fail to address), RSA has to sacrifice some degree of imaging precision without using the phase information[14]. As a result, our design seeks to identify the overall shape of an object surface (location, orientation, surface boundaries, material), rather than fine-grained details such as individual keys on a computer keyboard. *Second*, our design is unable to accurately image small objects. It can detect and locate a wrench handle (of 2.5cm width), but the detected width varies between 1cm to 5cm. It cannot locate a keyring because the reflection is too weak to be captured by our HXI radios. To recognize these small objects, one could

---

[13]Shape deviation is defined by the maximum difference between the actual object surface and the imaged object surface projected onto the object surface's principal axis.

[14]In practice, not requiring phase information can be an advantage, since most COTS radios do not report phase but only RSS values.

Ground truth				Detected Position			Detected Shape				
				Center location error		Orientation	Detected	Shape deviation		Width error	
Objects in Figure 3	Shape	Radius	Width	Median	Max	error (Max)	curvature	Median	Max	Median	Max
(a) Aluminum Jar	Convex	+10.0	10.00	4.55	8.11	0.29°	Convex	1.59	2.22	1.00	2.33
(b) Steel cylinder	Convex	+15.0	15.00	4.43	4.98	0.51°	Convex	1.46	1.78	1.03	1.88
(c) Curved steel surface	Convex	+29.0	21.21	7.26	9.47	0.69°	Convex	1.47	1.93	2.67	4.22
(d) Curved steel surface	Concave	−29.0	21.21	6.64	7.65	0.90°	Concave	-1.64	-1.59	1.21	1.79
(e) Curved steel surface	Convex	+23.0	22.63	5.51	7.37	1.05°	Convex	4.46	6.35	0.91	3.59
(f) Metal desktop front	Flat	+∞	06.72	2.82	3.64	0.49°	Flat	0.13	0.62	0.82	1.02
(g) Plastic keyboard	Flat	+∞	10.00	4.44	7.31	0.81°	Flat	0.16	0.36	2.69	4.16
(h) Cardboard box	Flat	+∞	18.00	4.31	5.13	0.72°	Flat	0.15	0.28	2.41	3.00
(i) Wood board	Flat	+∞	22.00	3.83	8.73	0.44°	Flat	0.43	0.68	3.09	4.17
(j) Plastic battery case	Flat	+∞	23.00	2.06	3.17	0.47°	Flat	0.28	0.48	1.70	3.51
(k) Plastic monitor	Flat	+∞	26.00	4.07	6.29	0.45°	Flat	0.10	0.11	0.64	1.06
(l) Metal desktop side	Flat	+∞	28.28	2.69	2.95	0.58°	Flat	0.12	0.12	1.78	3.16

Table 1: RSA imaging performance in terms of error in object center position and orientation, detected curvature type, deviation of overall shape, and error in object width (surface boundary). All the numbers are in the unit of *centimeter* except for the orientation error and curvature type.

Object (Material)	Estimated Reflection Loss	Top 3 Matches (out of 39)
Desktop (Metal)	0.3dB	**Metal**, Quartzite, Glass
Box (Cardboard)	6.1dB	**Cardboard**, Pertinax, Acrylic glass
Monitor (Plastic)	7.9dB	Chipboard, Fiberboard, **Plastic**
Board (Wood)	12.7dB	**Wood**, Brick, Breeze block
Cylinder (Metal)	0.3dB	**Metal**, Quartzite, Glass

Table 2: Results of RSA material detection.

use a stronger radio, or move TX and RX much closer to the object, *e.g.* <0.5m which becomes a near-field scenario and requires a new imaging design. *Third*, the accuracy of width estimation depends heavily on the RX movement distance. The amount of RX movement distance required to maintain high precision increases linearly with the sensing range and object size. We found that for our HXI testbed and all the test objects, 1 meter RX movement is sufficient. Our RX movement planning also predicts the same trajectory length (see §5).

6.4 Robustness to Noise

While Table 1 lists the imaging result when the TX/RX positioning error is bounded by $6cm$, we expand our noise model to explore RSA's noise tolerance. We found that RSA's performance is insensitive to trajectory errors when the deviation is bounded by $10cm$. Thus we focus on the TX/RX position errors. Specifically, we pick X as the maximum location error (deviation from the ground truth), draw a circle of radius X around the ground truth and randomly pick a point on the circle as TX's relative location to RX. We repeat this 20 times per X and report the maximum imaging errors. Using object (g) as an example, Figure 9 plots the maximum error in center location and width estimation for X between 0 and 20cm. We see that both errors grow gracefully with X, indicating that RSA is robust against TX/RX positioning errors. We observe this same trend for all objects.

6.5 RSA vs. SAR and unfocused SAR

We also compare RSA with SAR and unfocused SAR (as described by existing work [52]). Since both SAR algorithms do not offer curvature and material information, we only evaluate object center location error and width error. Specifically, for each scenario defined by TX/RX positioning error, RX trajectory, and the object, we compute the amount of error reduction achieved by RSA, *e.g.* $\frac{\text{width error (SAR)}}{\text{width error (RSA)}}$ or $\frac{\text{center location error (SAR)}}{\text{center location error (RSA)}}$. We report the min, median, and max values across the eleven objects, 10 trajectories and 20 in-

stances of position errors for a given range X. Because unfocused SAR is highly sensitive to the choice of RX movement distance, we use 0.5 meter for unfocused SAR (which provides the best overall performance across all the objects), and 1 meter for RSA and SAR.

Figure 10 lists the error reduction factor of RSA. For center point estimation, SAR and unfocused SAR have very similar performance [52], so we only report one. We see that RSA can effectively reduce the imaging error. This is particularly true for width estimation – the median reduction factor is 2-6.7 (over unfocused SAR) and 2.9-8.2 (over SAR); while the maximum value can reach 18 and 38 respectively. Also, width error reduction peaks at zero TX/RX position error, confirming RSA is highly robust against trajectory errors. Finally, RSA reduces errors in center point estimation by a factor of 1.2-2.32 (median). This is mostly due to the iterative search process (§4.6).

6.6 Microbenchmarks

RX Movement Distance. Figure 11 compares the object width error at different RX movement distances. We see that RSA follows the same trend as noise-free SAR: imaging error reduces with moving distance and gradually converges to a stable value. This aligns with the theoretical limit in Eq. (1) where increasing aperture (via RX movement) leads to higher imaging precision. Unfocused SAR, however, is highly sensitive to this parameter.

RSS Measurement Frequency. This factor translates into the choice of N, the number of measurements for a given movement distance. In practice, we want to minimize measurement frequency to save energy. Yet insufficient number of measurements reduces the accuracy of our model fitting. Our results in the above perform one measurement per 1cm. At a slow movement speed of 0.5m/s (1.1mph), the measurement frequency is once per 20ms. We found that the results remain the same even at a lower frequency of once per 80ms (*i.e.* once per 4cm).

Beam Steering Granularity. Using an electronically controlled mechanical rotator, our testbed can steer antenna beam in increments of 0.15°. While our experiments above use data from 1° steering, we also perform imaging under 0.15°, 3° and 5° steering to examine the impact of antenna hardware (steerable phased arrays). To separate its impact on localization, we use the same TX/RX localization result of 1° across all the experiments. Our results show that $1° - 3°$ steering is an efficient choice – increasing granularity to 0.15° reduces width error by $< 0.5cm$ while relaxing to 5° doubles the width error.
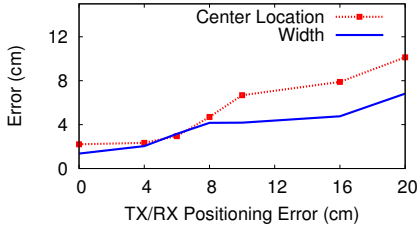
Figure 9: RSA's imaging errors scale gracefully with TX/RX position errors. RX trajectory noises are present for all the experiments.
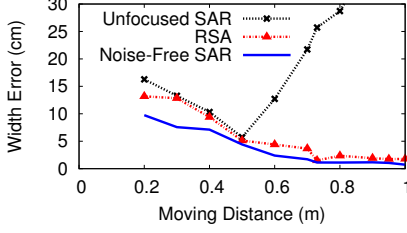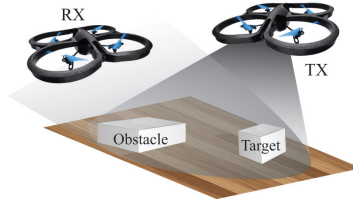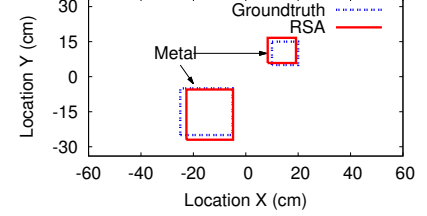
TX/RX Positioning Error (cm)	center location error (SAR) center location error (RSA)			width error (unfocused SAR) width error (RSA)			width error (SAR) width error (RSA)		
	Median	Min	Max	Median	Min	Max	Median	Min	Max
0	1.20	1.00	2.07	6.71	3.88	17.95	6.92	3.16	19.09
4	1.72	1.24	2.77	4.44	2.59	11.44	8.20	4.59	38.33
8	1.72	1.44	2.63	3.23	1.27	6.67	5.06	3.34	10.39
16	1.85	1.62	3.83	2.32	1.11	5.29	2.90	1.84	6.89
20	2.32	1.47	2.78	2.18	1.01	3.82	3.05	1.44	6.09

Figure 10: Comparing RSA to SAR and unfocused SAR in terms of the ratio of error under SAR (or unfocused SAR) and error under RAS. The RX trajectory errors are present in all the experiments. Since the performance of unfocused SAR is sensitive to RX moving distance, we configure it as 0.5 meter while SAR and RAS use 1 meter.

Figure 11: Impact of measurement configurations on RSA imaging performance, in terms of width error.

(a) Scenario setup

(b) Imaging result (top view)

Figure 12: "Realistic" case study of RSA imaging: a drone seeks to locate the small metal object while avoiding a nearby obstacle.

6.7 Case Study: Multiple Objects Detection

Consider a scenario in Figure 12(a), where a drone uses RSA imaging to locate an object, *i.e.* a square metal box of size 8cm×8cm. The target rests on a wood floor with a nearby larger (metal) object (size 18cm×18cm) as the obstacle. To locate (and pick up) the object, a drone needs to recognize both objects, with the help of another drone as TX.

With two testbed radios emulating drones, they first perform 60GHz localization to locate each other. They then coordinate to sense the objects. Since the two objects are in proximity they can be covered by a single TX beam. After TX focuses its beam on the two objects (and sends beacon signals), RX moves in two directions sequentially to determine location, curvature, width and height, and material. The visual imaging result and the ground truth are shown in Figure 12(b) where RSA recognizes two flat metal objects, their overall shape/size, and the wood floor in between.

7. RELATED WORK

Camera-based Imaging.   Camera is widely used for object recognition [16, 32, 33]. Detecting object position and shape, however, requires bulky, high-end cameras (*e.g.* Google's Project Tango requires an infrared depth camera and a fish-eye lens). These mechanisms require good visibility and cannot reliably identify object material. RSA takes a low-cost RF-based approach leveraging mobile networking chipsets, and its 60GHz reflected signals reveal key properties of the object surface without any light.

Sonar and Radar Systems.   These systems have been applied to many fields [43], from mapping terrain contour, tracking moving targets, to detecting concealed weapons at security checkpoints [17, 6, 10, 34, 42, 46]. They use special hardware like X-Ray or bulky lenses to achieve high precision, which are too large/expensive for mobile devices. RSA differs by using commodity 60GHz networking chipsets that are being integrated into today's mobile devices.

RF-based Systems.   Researchers have explored WiFi-band solutions to detect human motion, activity and gestures, and to detect (metal) objects [8, 7, 15, 36, 29, 40, 12]. A recent work built WiFi imaging using OFDM and large phased arrays (available on APs) and discussed the resolution limitation due to its large wavelength [25]. Our work considers 60GHz (mmwave) communications because it offers several desirable qualities for mobile imaging when compared with WiFi: tiny wavelength, high directionality, stable and predictable signal propagation. In addition to providing high-resolution (∼1-5cm), our imaging algorithm is also different by using just RSS measurements (rather than phase [25]) without requiring specialized hardware (*e.g.* [8, 7]). Our work was inspired by recent 60GHz radar designs [52, 44] that apply SAR to detect object surface location and boundary in absence of noise. Our work develops a new imaging solution that is robust against noise and also detects surface curvature and materials.

8. LIMITATIONS AND FUTURE WORK

Our proposed 60GHz mobile radar detects the location, orientation, curvature and surface boundaries of nearby objects using only signal strength measurements, and achieves cm-level precision.

Several limitations remain before we can realize a high precision, environmental mapping system using RF reflections. *First*, our imaging works when both TX and RX have line-of-sight to the target object because 60GHz signals cannot penetrate walls or most objects. To perform environmental mapping in 3D, TX and RX (*e.g.*, mobile devices) must have a way to intelligently navigate across space while coordinating their positions. *Second*, so far we only consider the general shape of static and regular object surfaces where reflected RSS is stable over time and predictable via a model. For moving or irregular objects, *e.g.*, humans, and detailed shape, *e.g.*, keys on keyboard, we need new models to define the correlation between object shape and reflected signal patterns. *Finally*, we need to develop an algorithm for TX and RX to reliably and iteratively scan individual surfaces while moving in unknown environments. Such schemes must be robust and work reliably in large environments with complex objects (*e.g.* caves, collapsed tunnels).

9. REFERENCES

[1] HP Elite x2 1011 G1 Datasheet. http://www8.hp.com/us/en/ads/elite-products/elitex2-1011.html.

[2] IEEE 802.11 Task Group AD. http://www.ieee802.org/11/Reports/tgad_update.htm.

[3] Meet the drones patrolling Barcelona's sewers. http://www.cnet.com/news/meet-the-drones-patrolling-the-pipes-of-barcelonas-sewers/.

[4] Sensor fusion on android devices: A revolution in motion processing. http://davidcrowley.me/?p=370.

[5] Draft standard - part 11: Wireless lan medium access control (mac) and physical layer (phy) specifications - amendment 4: Enhancements for very high throughput in the 60ghz band. IEEE P802.11adTM/D9.0, July 2012.

[6] ADAMS, C., HOLBROOK, D., AND SENGSTEN, R. A handheld active millimeter wave camera. In *Technologies for Homeland Security (HST), 2010 IEEE International Conference on* (2010).

[7] ADIB, F., KABELAC, Z., KATABI, D., AND MILLER, R. C. 3d tracking via body radio reflections. In *Proc. of NSDI* (2014).

[8] ADIB, F., AND KATABI, D. See through walls with wi-fi! In *Proc. of SIGCOMM* (2013).

[9] AL-SALIHI, N. Precise positioning in real-time for visually impaired people using navigation satellites. *International Journal of Engineering and Technology 12*, 2 (2010), 83–89.

[10] APPLEBY, R., AND ANDERTON, R. Millimeter-wave and submillimeter-wave imaging for security and surveillance. *Proceedings of the IEEE* (2007), 1683–1690.

[11] BAHL, P., AND PADMANABHAN, V. N. Radar: An in-building rf-based user location and tracking system. In *Proc. of INFOCOM* (2000).

[12] BHARADIA, D., JOSHI, K. R., AND KATTI, S. Full duplex backscatter. In *Proc. of HotNets* (2013).

[13] CHAN, Y. K., AND KOO, V. C. An introduction to synthetic aperture radar (sar). *Progress in Electromagnetics Research B* (2008), 27–60.

[14] CHENEY, M., AND BORDEN, B. *Fundamentals of Radar Imaging*, vol. 79. SIAM, 2009.

[15] CHETTY, K., SMITH, G. E., AND WOODBRIDGE, K. Through-the-wall sensing of personnel using passive bistatic wifi radar at standoff distances. *Trans. on Geoscience and Remote Sensing 50*, 4 (2012), 1218–1226.

[16] DAVISON, A. J., REID, I. D., MOLTON, N. D., AND STASSE, O. Monoslam: Real-time single camera slam. *Trans. on Pattern Analysis and Machine Intelligence* (2007).

[17] FEDERICI, J. F., GARY, D., BARAT, R., AND ZIMDARS, D. Thz standoff detection and imaging of explosives and weapons. In *Proc. of Defense and Security* (2005).

[18] FRICKE, A., REY, S., ACHIR, M., LE BARS, P., KLEINE-OSTMANN, T., AND KURNER, T. Reflection and transmission properties of plastic materials at thz frequencies. In *Proc. of IRMMW-THz* (2013).

[19] FRIIS, H. T. A note on a simple transmission formula. *In Proc. of IRE 34*, 5 (1946), 254–256.

[20] GRAJAL, J., BADOLATO, A., RUBIO-CIDRE, G., UBEDA-MEDINA, L., MENCIA-OLIVA, B., GARCIA-PINO, A., GONZALEZ-VALDES, B., AND RUBINOS, O. 3-d high-resolution imaging radar at 300 ghz with enhanced fov. *Microwave Theory and Techniques, IEEE Transactions on 63*, 3 (March 2015).

[21] GU, F., ZHANG, Q., LOU, H., LI, Z., AND LUO, Y. Two-dimensional sparse synthetic aperture radar imaging method with stepped-frequency waveform. *Journal of Applied Remote Sensing 9*, 1 (2015).

[22] GUERRERO, L. A., VASQUEZ, F., AND OCHOA, S. F. An indoor navigation system for the visually impaired. In *Proc. of Sensors* (2012).

[23] HALPERIN, D., KANDULA, S., PADHYE, J., BAHL, P., AND WETHERALL, D. Augmenting data center networks with multi-gigabit wireless links. In *Proc. of SIGCOMM* (2011).

[24] HECHT, E. *Optics*. Addison-Wesley, 2002.

[25] HUANG, D., NANDAKUMAR, R., AND GOLLAKOTA, S. Feasibility and limits of wi-fi imaging. In *Proc. of SenSys* (2014).

[26] JUDS, S. *Photoelectric Sensors and Controls: Selection and Application, First Edition*. Taylor & Francis, 1988.

[27] KOO, V. C., LIM, T. S., AND CHUAH, H. T. A comparison of autofocus algorithms for sar imagery. In *Proc. of PIERS* (2005).

[28] KULPA, K., PURCHLA-MALANOWSKA, M., AND MALANOWSKI, M. P. Improvement of resolution in real-time unfocused sar algorithm. In *Proc. of EuSAR* (2004).

[29] KUMAR, S., GIL, S., KATABI, D., AND RUS, D. Accurate indoor localization with zero start-up cost. In *Proc. of MobiCom* (2014).

[30] LANGEN, B., LOBER, G., AND HERZIG, W. Reflection and transmission behavior of building materials at 60ghz. In *Proc. of PIMRC* (1994).

[31] LINE, M. Robot rescue: First-responders of the future. FoxNews.com, June 2014.

[32] LOWE, D. G. Object recognition from local scale-invariant features. In *Proc. of ICCV* (1999).

[33] LOWE, D. G. Distinctive image features from scale-invariant keypoints. *International journal of computer vision 60*, 2 (2004).

[34] MACKENZIE, J., AND BROWN-KENYON, E. Wide-bandwidth mobile radar for isar/sar radar imaging. In *IEE Colloquium on Radar and Microwave Imaging* (1994).

[35] MADRIGAL, A. C. The trick that makes google's self-driving cars work. The Atlantic, May 2014.

[36] MOSTOFI, Y. Cooperative wireless-based obstacle/object mapping and see-through capabilities in robotic networks. *IEEE TMC 12*, 5 (2013), 817–829.

[37] MÜLLER, M. *Information Retrieval for Music and Motion*. Springer Berlin Heidelberg, 2007.

[38] NIESSNER, M., DAI, A., AND FISHER, M. Combining inertial navigation and icp for real-time 3d surface reconstruction. In *Proc. of Eurographics* (2014).

[39] PENG, C., SHEN, G., ZHANG, Y., LI, Y., AND TAN, K. Beepbeep: a high accuracy acoustic ranging system using cots mobile devices. In *Proc. of SenSys* (2007).

[40] PU, Q., GUPTA, S., GOLLAKOTA, S., AND PATEL, S. Whole-home gesture recognition using wireless signals. In *Proc. of MobiCom* (2013).

[41] QIU, X., DING, C., AND HU, D. *Bistatic SAR Data Processing Algorithms*. Wiley, 2013.

[42] SATO, M., AND MIZUNO, K. *Millimeter-wave imaging sensor*. InTech, 2010.

[43] SCHEER, J. A., AND MELVIN, W. L. *Principles of modern radar*. The Institution of Engineering and Technology, 2013.

[44] SEO, M., ANANTHASUBRAMANIAM, B., MADHOW, U., AND RODWELL, M. J. Millimeterwave (60 ghz) imaging wireless sensor network: Recent progress. In *Proc. of ACSSC* (2007).

[45] SHANKLAND, S. Wilocity: 2015 phones getting extra-fast 802.11ad networking. CNet, February 2014.

[46] TSENG, T.-F., WUN, J.-M., CHEN, W., PENG, S.-W., SHI, J.-W., AND SUN, C.-K. High-resolution 3-dimensional radar imaging based on a few-cycle w-band photonic millimeter-wave pulse generator. In *Proc. of OFC* (2013).

[47] VALDES-GARCIA, ET AL. Single-element and phased-array transceiver chipsets for 60-GHz Gb/s communications. *IEEE Communications Magazine 49*, 4 (April 2011), 120 –131.

[48] ZHANG, H., VENKATESWARAN, S., AND MADHOW, U. Channel modeling and mimo capacity for outdoor millimeter wave links. In *Proc. of WCNC* (2010).

[49] ZHANG, Z., CHU, D., CHEN, X., AND MOSCIBRODA, T. Swordfight: Enabling a new class of phone-to-phone action games on commodity phones. In *Proc. of MobiSys* (2012).

[50] ZHOU, X., ZHANG, Z., ZHU, Y., LI, Y., KUMAR, S., VAHDAT, A., ZHAO, B. Y., AND ZHENG, H. Mirror mirror on the ceiling: Flexible wireless links for data centers. In *Proc. of SIGCOMM* (2012).

[51] ZHU, Y., ZHANG, Z., MARZI, Z., NELSON, C., MADHOW, U., ZHAO, B. Y., AND ZHENG, H. Demystifying 60GHz outdoor picocells. In *Proc. of MobiCom* (2014).

[52] ZHU, Y., ZHU, Y., ZHANG, Z., ZHAO, B. Y., AND ZHENG, H. 60GHz mobile imaging radar. In *Proc. of HotMobile* (2015).

[53] ZHURBENKO, V. *Electromagnetic Waves*. InTech, 2011.